Macromolecular Materials and Engineering
www.mme-journal.de

Polystyrene Foam with High Cell Density and Small Cell Size by Compression-Injection Molding and Core Back Foaming Technique: Evolution of Cells in Cavity

Tiantian Bai, Binbin Dong, Mengjun Xiao, Hu Liu,* Ning Wang, Yaming Wang, Chao Wang, Chuntai Liu, Wei Cao, Jiaoxia Zhang, Yong Ma, and Zhanhu Guo**

Many efforts have been made to obtain uniform cell structures from foam injection molding techniques. However, cell nucleation mechanism and complex dynamics during the cell formation have rarely been well understood. Here, high-pressure foam injection molding (HPFIM) is achieved by combining the injection–compression molding with core back foaming (ICMCBF) technique. The influences of compression pressure and time on the cell structure of polystyrene foam during the foaming process are studied. Compared with low pressure for conventional foam injection molding, high compression pressure (200 bar) and fast pressure drop rate of ICMCBF endow the foam with the highest cell density (1.59×10^7 cells cm^{-3}), and the smallest cell size (15 μm). The tensile strength and impact strength are enhanced by about 60% (from 22.3 to 35.6 MPa) and 80% (from 3.6 to 6.8 MPa), respectively. This study gives a critical understanding of the cell nucleation and growth mechanism of the foam injection molding and supplies a new strategy for the fabrication of foam with uniform cell structure.

1. Introduction

Recently, faced with global energy crisis and environmental pollution, both industries and academics have made efforts to manufacture new-generation lightweight products by using less raw material and consuming less energy.[1–11] Conventional foam injection molding (CFIM) technology is achieved by injecting the mixture of polymer melt and supercritical fluid (SCF) into a closed mold cavity with a short-shot, and the expandable melt/gas mixture generates a foam structure under low pressure.[12–18] However, it is known that the differences of shearing stress and temperature in both the direction of the flow and the direction perpendicular to the flow usually result in a nonuniform cell structure, which deteriorates the mechanical properties of the foamed products.[13,19–24] In this regard, the effects of processing parameters (e.g., injection speed, melt temperature, shot size, and the dosage of SCF) on the cell structure have been extensively researched.[25–28] Besides, the effect of the fillers on the cell nucleation was also studied.[25–27] For example, Lee et al.[29] optimized the processing parameters systematically, including the injection flow rate, blowing agent content, and melt temperature in CFIM, and achieved structural foams with a high void fraction and improved structure uniformity. By increasing the shot size, Wang et al.[23] observed the shift from elongated cells into circular cells in the direction parallel to the flow in the FIM. In addition, FIM can sometimes be accompanied by a controlled mold-opening step which is also termed as breathing or core-back to increase the void fraction.[30–32] For example, Takeshi et al.[33] had experimentally confirmed the disappearance of

T. Bai, Prof. B. Dong, M. Xiao, Prof. H. Liu, Prof. Y. Wang, Prof. C. Liu, Prof. W. Cao
National Engineering
Research Center for Advanced Polymer Processing Technology
Zhengzhou University
Zhengzhou, Henan 450002, China
E-mail: dongbinbin@zzu.edu.cn; liuhu@zzu.edu.cn

H. Liu, Dr. J. Zhang, Dr. Y. Ma, Prof. Z. Guo
Integrated Composites Laboratory
Department of Chemical and Biomolecular Engineering
University of Tennessee
Knoxville, TN 37996, USA
E-mail: zguo10@utk.edu

The ORCID identification number(s) for the author(s) of this article can be found under https://doi.org/10.1002/mame.201800110.

DOI: 10.1002/mame.201800110

Prof. N. Wang
State Key Laboratory of Marine Resource Utilization in South China Sea
Hainan University
Haikou 570228, China

Dr. C. Wang
College of Materials Science and Engineering
North University of China
Taiyuan 030051, China

Dr. J. Zhang
School of Material Science and Engineering
Jiangsu University of Science and Technology
Zhenjiang, Jiangsu 212003, China

Dr. Y. Ma
College of Materials Science and Engineering
Shandong University of Science and Technology
Qingdao 266590, China

cells when the cavity was fully packed and the cell nucleation was observed again when the mold plate was moved and the cavity pressure dropped.

However, unlike the batch foam in a static condition, FIM contains a complex behavior of fountain flow, resulting in different cell nucleation time and then different melt conditions for cell growth under different shearing history. Hence, it is difficult for FIM to form a uniform and stable cell structure.[23,24] However, with a high packing pressure after a full-shot in the high-pressure foam injection molding (HPFIM), uniform and stable cell structures were formed with the cell nucleation and growth occurring during the shrinkage and solidification of polymer melt.[34,35] For example, Shaayegan et al.[36] studied the mechanism of cell nucleation and growth in HPFIM through in situ visualization. The packing pressure and packing time were found to be very important for re-dissolving the gate-nucleated cells. However, due to the complexity of the melt flow and cell dynamics in FIM, the mechanisms of cell nucleation and growth still need to be investigated further.

For the CFIM technology which is foamed in low pressure, the homogeneous melt/gas mixture is injected into a closed cavity. As the mixture enters the mold cavity, the pressure drop of the polymer/gas mixture causes the nucleation. Then the expandable melt generates a foamed specimen as it is cooled down.[37,38] The nucleation mechanism strongly depends on the FIM process, such as the type and amount of the blowing agent and the nucleating agent, and the resistance of the gate.[36] In FIM, the cell nucleation generally occurs under a high pressure drop when the melt/gas mixture flows across the gate and fills in the closed mold cavity.[38] For example, Lee et al.[29] achieved a high void fraction up to 35% in the FIM process using a short-shot, but the cell structure suffered from a considerable nonuniformity at different locations of the foamed part. Although a full-shot was used in HPFIM, the cells still suffered from a considerable nonuniformity because of the strong shear in the filling stage (**Figure 1**a,b). Further, this phenomenon is associated with different nucleation rates, deformation, and coalescence of cells during the filling. First, it is challenging to maintain a constant cell nucleation rate. That is to say, because of the differences of nucleation time, pressure, and temperature history during their travel toward the end of the cavity, the cells with different sizes are constructed.[39–41] Due to large shearing and stretching involved in the filling process of FIM, severe deformation and even coalescence of growing cells are observed.[22,39,41,42] Hence, short injection time by rapid filling may decrease the nucleation during the filling and results in a more uniform cell structure with less deformed cells in CFIM.

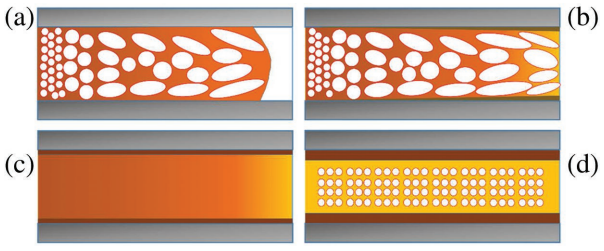

Figure 1. Ideal HPFIM process: a) mold filling and the formation of gate-nucleated cells due to pressure drop over the gate; b) full-shot; c) collapse and dissolution of gate-nucleated cells; d) nucleation and growth of new cells due to the melt shrinkage.

In contrast, a uniform cell structure can be achieved in HPFIM. A HPFIM is schematically illustrated in Figure 1. Generally, the cell nucleation occurs during the whole filling stage, which is similar to CFIM. Ideally, these nucleated cells may completely dissolve back to melt under the high packing pressure of the mold cavity (Figure 1c). The driving force for cell nucleation in this process is provided by volume shrinkage during the melt solidification after injection. Then new foam process occurs, and a uniform cell structure can be achieved (Figure 1d).[36]

It was observed that the required packing pressure increased with increasing the injection speed, the resistance of the gate, and the content of the blowing agent. However, the application of the packing pressure may cause heterogeneous structures in the direction of the flow, although the combination of packing pressure and packing time is sufficient to re-dissolve the cells.[43] Injection–compression molding is a technique which will cause a quick increase of cavity pressure after filling through a controlled mold compression in the injection molding.[44,45] In the normal core-back process, the cavity generally expands in the direction perpendicular to the flow for a certain distance at a set opening speed, once the filling stage is completed.[36,46,47] For the technology of core-back, a fast pressure drop in cavity can be achieved easily. For example, Huang et al.[48] obtained a more uniform cellular structure with smaller sizes using injection–compression molding. Besides, it is known that numerical simulation is an effective way to learn and analyze the injection molding process,[49,50] especially the foam injection molding.[22,51–53]

In this article, the process of injection–compression molding followed by a core back foaming (ICMCBF) technique was applied to realize HPFIM using polystyrene (PS) and N_2 as an example. The foam fracture surfaces of CFIM and ICMCBF samples were observed to analyze the cell morphology. The cell density, diameter, diameter distribution, and thickness of foamed layer were counted. Generally, temperature and viscosity in the mold cavity are both crucial but hard to be obtained from experiments. Hence, the temperature and viscosity distribution in the whole thickness were studied by simulating the filling and cooling stages of CFIM process with the commercial software of Moldflow to match the real thickness of foamed layer. Meanwhile, the evolution of the cell in cavity was investigated using the temperature and pressure sensors. Finally, the tensile and impact properties were conducted to investigate the relationships between the cell structure and the mechanical performance.

2. Experimental Section

2.1. Equipment and Materials

A mold with a movable template was designed and manufactured, so that the thickness of the cavity could be changed to obtain a relatively high pressure inside the mold cavity by mold compression after filling. To capture the temperature and

Table 1. Details of processing parameters in CFIM.

Parameters	Values
Injection temperature [°C]	225, 230*, 235
Injection speed [cm^3 s^{-1}]	40, 60*, 80
Back pressure [bar]	80, 100*, 120
Shot size [%]	85, 91, 96*
Dosage of SCF [%]	0.5, 0.6*, 0.7
Mold temperature [°C]	50*

Note: the cell structure of CFIM sample with the parameters labeled with "*" are showen in Fig 3, 4, 5 and 6.

pressure profiles inside the cavity, sensors from PRIAMUS were mounted in the mold. The pressure sensor was mounted at a third of the mold cavity close to the gate and the temperature sensor was mounted close to the end of the mold cavity. All the sensors were connected to a computer to record the pressure and temperature during the whole molding cycles.

A 220-ton Arburg ALLROUNDER 570S injection molding machine equipped with a Trexel Mucell SCF delivery system was used to conduct the FIM experiments. A rectangular mold cavity with a nominal dimension of 160 mm × 100 mm × 3.5 mm (the thickness is variable), fed by a fan gate with a thickness of 2 mm, was used.

PS (PG33, MFI = 7.9 g 10 min^{-1}, 200 °C, 5 kg) purchased from Zhenjiang CHIMEI Chemistry was blown using industrial nitrogen (N_2) with a purity of 99.9%.

2.2. Experimental Procedures and Processing Conditions

A series of CFIM and ICMCBF experiments were conducted under different conditions. Their pressure and temperature profiles in the mold cavity were recorded. The effects of injection temperature, injection speed, back pressure, shot size, and the dosage of SCF on the cell structure of CFIM were investigated first and the specific parameters are shown in **Table 1**. Considering the fine cell structure, samples with parameters labeled with "*" in Table 1 were chosen to be compared with HPFIM.

As shown in **Figure 2**, an almost full-shot (96%) was applied during the filling stage of ICMCBF. After that, mold compression under a certain pressure and a certain time was conducted after filling to re-dissolve the gate-nucleated cells. A fully filled mold cavity and a high melt pressure will be obtained by the compression pressure to achieve HPFIM. Then, the movable

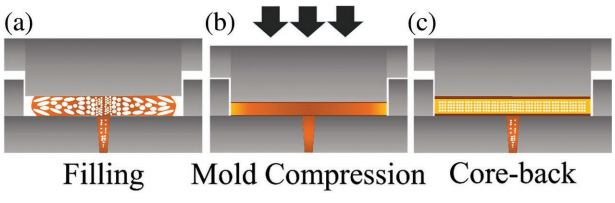

Figure 2. Ideal HPFIM process by ICMCBF: a) mold filling and the formation of gate-nucleated cells due to pressure drop over the gate; b) collapse and dissolution of gate-nucleated cells by mold compression; c) nucleation and growth of new cells by core-back.

Table 2. Details of processing parameters in ICMCBF.

Parameters	Values
Injection temperature [°C]	230
Injection speed [cm^3 s^{-1}]	60
Back pressure (bar)	100
Shot size [%]	96
Dosage of SCF [%]	0.6
Mold temperature [°C]	50
Core-back speed [mm s^{-1}]	2
Core-back amount [mm]	1
Compression pressure [bar]	0, 100, 200, 300
Compression time [s]	0, 3, 5, 7

Note: The compression pressure was calculated by dividing force by the projected area.

mold template went back to the pristine position to achieve new foam (Figure 2c). Using the aforementioned method, ICMCBF was successfully developed. Based on the process of CFIM, the parameters during melt mixing and filling stage were the same as the counterparts of CFIM. Meanwhile, the effects of compression pressure and time on the cell structure and mechanical performance were studied. Details of processing parameters of ICMCBF are shown in **Table 2**.

2.3. Foam Structure Characterization

According to ASTM D854-02, the normalized density of the foamed sample and the density of the solid sample were measured using a density meter with Equation (1):

$$\rho_f = \frac{m_1 \rho_1}{m_1 - m_2} \tag{1}$$

where m_1 is the mass of the sample in the air, m_2 is the mass of the sample in the water, and ρ_1 is the density of testing liquid. Both m_1 and m_2 were measured in gram. All the normalized densities were measured with a square block of 30 × 30 mm cut from the injection molding part which was located in one third of the mold cavity (with respect to the location of pressure sensor).

The cell morphology of the foamed samples was analyzed by using scanning electron microscopy (SEM, Zeiss Supra 55). The image processing was carried out using Image-Pro Plus software. The cell density of samples in CFIM and ICMCBF was obtained from the calculation of the circular cells in the SEM pictures vertical to the direction of the melt flow. Then the magnification of SEM was adjusted to obtain a picture of the core region with about 150–300 cells. Note that all the cell densities and sizes are calculated from at least three pictures. The cell density of each sample was then measured from SEM micrographs by using Equation (2).[54]

$$\text{Cell Density} = \left(\frac{nM^2}{A}\right)^{\frac{3}{2}} \times \frac{\rho_s}{\rho_f} \tag{2}$$

where n is the number of cells in the micrograph, A and M are the area and magnification factor of the micrograph in cm^2, ρ_s and ρ_f are the density of the solid and foamed samples.

2.4. Tensile and Impact Property Testing

According to the GB/T 1040.2-2006 and GB/T 1043-93, the dog-bone and strip-shaped specimens were cut from the middle part of the injection-molded part to conduct the mechanical property testing. The tensile samples with a gauge length of 25 mm and a width of 5 mm were conducted with a crosshead speed of 1 mm min^{-1} using a universal testing instrument (SHIMADZU AG-IC 50 kN) at room temperature. The impact samples with a length of 80 mm and a width of 10 mm were tested using the impact testing machine (MST Systems) at room temperature.

Different CFIM and ICMCBF products were conducted for tensile and impact property testing, respectively. The foamed specimens were placed in an atmospheric environment to diffuse gas for more than 1 month before the mechanical testing. For each sample, the average value reported was derived from at least five specimens.

3. Results and Discussion

3.1. Cell Structure of CFIM and ICMCBF Foam

CFIM experiments under different melt temperature, injection speed, backpressure, shot size, and SCF dosage were conducted to obtain a fine cell structure. Based on the parameters for CFIM, ICMCBF experiments were also investigated. The cell structures of CFIM and ICMCBF samples were studied systematically. Despite the same shot size (96%), the cell structures of CFIM and ICMCBF showed obvious differences.

As shown in **Figures 3** and **4**, the morphologies of the cross section vertical and parallel to the direction of the flow were

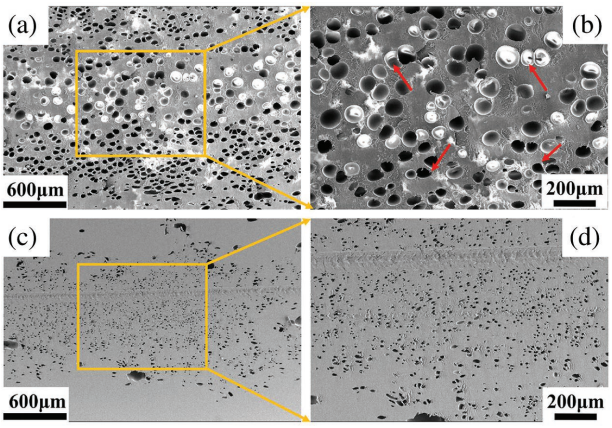

Figure 3. SEM images of samples for: a) CFIM-V and b) its high magnification-V (their parameters are labeled with "*" in Table 1); c) ICMCBF-V and d) its high magnification-V (compression pressure and time are 200 bar and 5 s) (V indicates the cross section which is vertical to the direction of the melt flow).

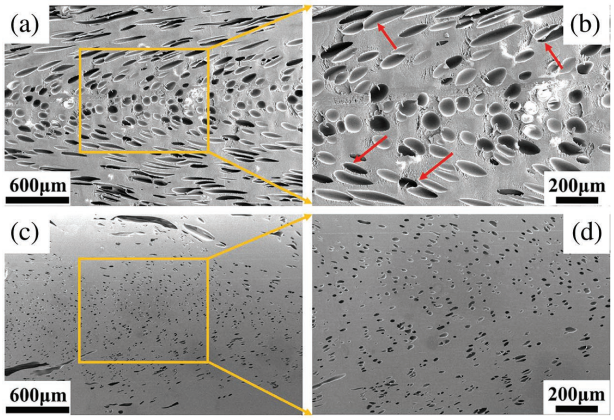

Figure 4. SEM images of samples for: a) CFIM-P and b) its high magnification-P (their parameters are labeled with "*" in Table 1); c) ICMCBF-P and d) its high magnification-P (compression pressure and time are 200 bar and 5 s) (P indicates the cross section which is parallel to the direction of the melt flow).

observed to get a total understanding of the cell structure of CFIM and ICMCBF samples. The cells exhibit round shape in the vertical direction (Figure 3b), but many deformed cells (Figure 4b) are found due to the characteristic of shear flow of polymer melt in the cavity. According to this phenomenon, it can be concluded that most of the cells are extremely stretched and sheared during the filling stage in CFIM. As discussed above, the gate-nucleated cells nucleate and grow in a dynamic condition while a relatively static condition can be achieved during the nucleating and growing of new cells after the re-dissolution of gate-nucleated cells. Wang et al.[23] proposed that the gas separation from polymer in stationary state will induce a perfect spherical structure due to isotropic characteristics after the filling stage or in the cooling stage. Consequently, under the static melt, cells with little deformation exist in the ICMCBF samples instead of the deformed ones in CFIM. Thus, the cells look nearly the same in the cross sections from both the vertical and parallel directions as shown in Figures 3d and 4d.

To further reveal the distinction of cell structure between CFIM and ICMCBF, the cell density and average cell diameter were counted. Their cell size distribution is shown in **Figure 5**. Notable high cell density and small average cell diameter were obtained for ICMCBF compared to CFIM. For instance, the cell density of ICMCBF sample is 1.59×10^7 cells cm^{-3}, which is about one order of magnitude higher than that of the CFIM sample (1.72×10^6 cells cm^{-3}). Meanwhile, the average cell diameter is significantly reduced from 60 to 15 μm. In addition, remarkable stable size distribution can also be observed for the ICMCBF sample compared to CFIM sample (Figure 5). For example, the average cell diameter of CFIM sample is 60 μm, but with a decentralized distribution ranging from 10 to 100 μm. However, the ICMCBF sample exhibited a small average diameter with a centralized distribution ranging from 5 to 20 μm. In short, higher density, smaller average size, and more uniform cells were obtained for ICMCBF samples. This can be explained on the basis of researches of Shaayegan et al.[36] and Sun et al.[55,56]: the nucleation rate showed a close relationship with the pressure drop rate. In CFIM, the melt

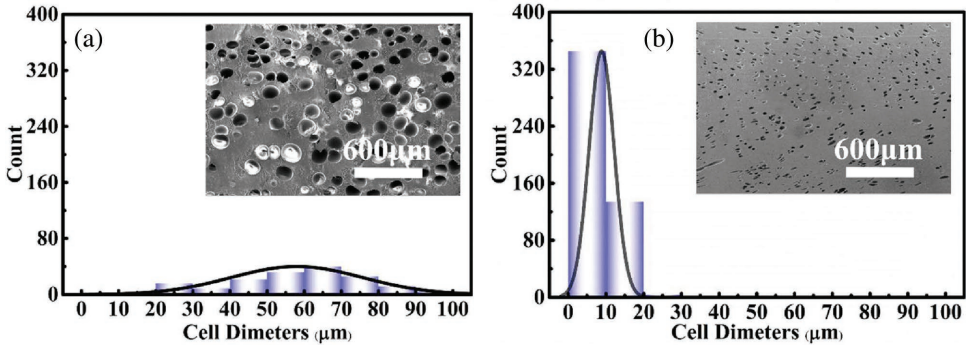

Figure 5. Distribution of cell diameters of a) CFIM (their parameters are labeled with "*" in Table 1) and b) ICMCBF samples (compression pressure and time are 200 bar and 5 s).

pressure decreases gradually along the cavity and eventually goes below the gas solubility pressure. Hence, a low pressure drop rate results in a small cell nucleation rate. In ICMCBF, a high melt pressure was endowed by mold compression and the pressure was unloaded at a very short time. Thus, a high pressure drop rate induced a high cell nucleation rate. Meanwhile, the competition between numerous nucleated cells, which grew at the same time, resulted in small cells. Besides, the relatively static condition and a high nucleation rate induced a more uniform cell size distribution when compared with the CFIM and ICMCBF samples.

In addition, different cell structures of CFIM and ICMCBF resulted in different densities for the foam parts. The shot sizes for CFIM and ICMCBF are both 96%. That is to say, the weight reduction of the foamed parts (including the runner and sprue system) fabricated by different processes is almost the same. Despite that, the normalized density for CFIM and ICMCBF measured by density meter showed that the density of CFIM samples (about 0.85 g cm^{-3}) was lighter than that of ICMCBF (about 0.99 g cm^{-3}). The reason for this mismatch between weight reduction and foam density may be related to the cell density, cell size, and inhomogeneity in the whole sample.

3.2. Thickness of the Foamed Layer of CFIM and ICMCBF

As shown in **Figure 6**, samples with typical sandwich structure were achieved in both CFIM and ICMCBF samples, which consisted of foamed core layer and nonfoamed skin layers.[[24]] The thickness of foamed layer was calculated from micrographs, and the ratios of thickness of foamed layer to the whole thickness were calculated in average. The results indicated that the foamed layer was about 45% in ICMCBF, which was lower than that in CFIM (81%). Generally, the formation of the compact skin layer was attributed to the instantaneous solidification of the polymer melt when it contacted the cavity wall. While Wang et al. proposed that the formation of final compact skin layer can be divided into two stages, that is, the filling stage and the cooling stage.[23] In the filling stage, the extremely deformed cells or filamentous cells have large interfaces between the gas and the polymer melt than the spherical cells, which is easy to re-dissolve the gas into polymer melt. In the cooling stage, because of the pressure drop of the material system caused by the shrinkage of polymer melt, the re-dissolved gas in the compact skin layer foamed during the filling stage may be separated from the polymer melt again. This phenomenon will produce spherical cells in the compact skin layer, which decrease the thickness of the skin layer forming in the filling stage. In Figure 6a,b , the dotted arrows indicate the spherical cells in both the vertical and parallel directions of the flow. These new cells expanded the foamed layer and reduced the skin layer. All these resulted in a thick foamed layer for the samples of CFIM.

Meanwhile, it can be seen from Figure 6c,d, that the counterpart of ICMCBF has a thinner foamed layer and thicker skin layers compared with the sample of CFIM. The differences of cell structures are mainly caused by the variation of pressure and temperature in the mold cavity. For cavity pressure, a proper time of high pressure caused by mold compression redissolved most filling cells into polymer melt and the following fast pressure drop drove the gas separated out from the melt. However, the temperature in the mold decreased rapidly during the mold compression.

The profiles of temperature and viscosity distribution in the direction of thickness were obtained from the filling and cooling simulation of Moldflow, and the material and processing conditions were almost the same as the real condition for CFIM (**Figure 7**). Among these two pictures, Figure 7a reflects the temperature and viscosity distribution at the filling end in the CFIM cycle. It is observed that the temperature in the center is a little higher than the injection temperature (230 °C) due to the gate shear effect. In addition, a wide high-temperature (higher than 150 °C) area appeared due to the short injection time. As we know, higher temperatures induce a lower viscosity (lower than 10^4 Pa·s) of the melt. The wide high-temperature and low-viscosity region (almost 80%) contributed to the thick foamed layer (almost 81%) in the CFIM. Figure 7b reflects the temperature and viscosity distribution in the whole thickness at the time after mold compression. Contrary to CFIM, a notably narrower high temperature and low viscosity region existed at the moment after mold compression, with large quantity of heat being dissipated. As discussed earlier, nucleation was triggered by the pressure drop after compression, but the low temperature at this time depressed the nucleation of cells. As a result, the narrow high temperature and low viscosity region (about 50%) induced the formation of thin foamed layer (45%). In short, different temperature

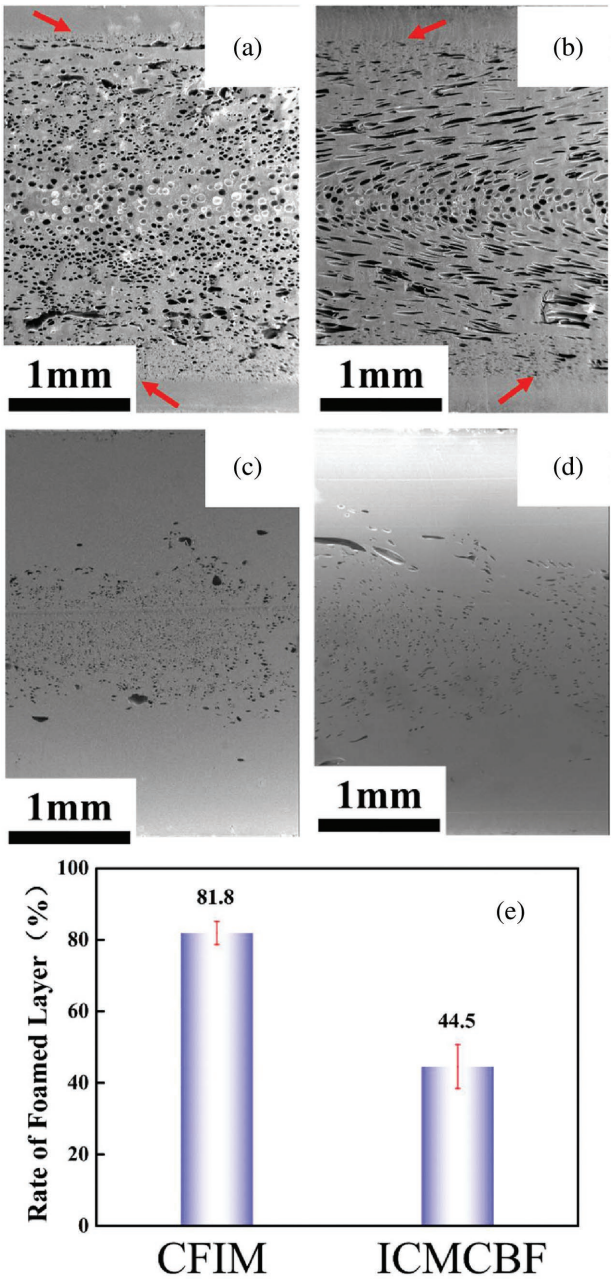

Figure 6. SEM images of sandwich structure in a) CFIM-V, b) CFIM-P (parameters are labeled with "*" in Table 1), c) ICMCBF-V, d) ICMCBF-P (compression pressure and time are 200 bar and 5 s), e) thickness of foamed layer for CFIM and ICMCBF sample (V and P indicate the cross sections which are vertical and parallel to the direction of the melt flow).

and viscosity distribution in the thickness after compression in ICMCBF are the key factors for the formation of a narrow-foamed layer compared to CFIM.

3.3. Effects of Compression Pressure and Time on Cell Structure

According to the investigation above, it can be concluded that an appropriate pressure after filling could induce uniform fine cells in the ICMCBF. Then, the influences of compression pressure and time on the foam structure were investigated systematically. **Figure 8** shows the ICMCBF cell structures under different compression pressure and 5 s compression time, including the images of cross section vertical and parallel to the direction of the melt flow. **Figure 9** shows their corresponding cell density and cell size. From the SEM images of the cell density and size, the cell structures of ICMCBF under different compression pressures were investigated. When the compression pressure was set as 100 bar, the deformed cells and obvious flow mask still exist in the final structure. Thus, 100 bar is insufficient to re-dissolve the gate-nucleated cells, resulting in a lower cell density and a smaller cell size than CFIM. When the compression pressure was increased to 200 bar, most of the deformed cells were absent and replaced by numerous new cells, indicating that the 200 bar compression pressure was enough to re-dissolve the gate-nucleated cells into the melt. After that, core-back process caused a fast pressure drop, which induced a high nucleation rate, thus a large number of cells nucleated and grew at the same time. These cells could not grow as large as the ones in the CFIM because of the competition between them. Similarly, a much higher compression pressure of 300 bar could effectively re-dissolve the gate-nucleated cells as new un-deformed cells were observed in the SEM images as well.

Figure 10 shows the ICMCBF cell structures under a compression pressure of 300 bar (which was proved to be high enough to re-dissolve the filling cells) and different compression time. **Figure 11** statistically shows the cell density and cell structure. The effects of compression time on the cell density and size of ICMCBF were analyzed by SEM. Similarly, when the compression time was 3 s, the deformed cells were difficult to be re-dissolved in the melt and the obvious flow mask still existed in the final structure. As the compression time was increased to 5 s, new cells and more nucleation occurred in a relatively static condition. However, the cell density and size showed a decreasing tendency when the compression time was further increased.

3.4. The Cavity Pressure and Temperature During Injection Molding

Figure 12 shows the evolution of pressure and temperature in the mold cavity during the whole injection molding cycle. As discussed in Section 2, the pressure sensor was mounted at a third of the mold cavity close to the gate and the temperature sensor was mounted close to the end of the mold cavity. In each cycle, the sensors began to record the pressure and temperature according to the signal of proximity switch. After the complete close of mold and the open of nozzle, the filling stage began. When the front of polymer melt arrived at the position of the pressure sensor, a high pressure was tested by the pressure sensor. The pressure grew fast to a high pressure and then descended quickly during the filling stage. After that, the temperature increased sharply once the melt reached the end of the cavity and then decreased slowly with the prolongation of time. Consequently, the pressure profiles grew fast to a high pressure from 0 to about 4 s during each cycle, indicating

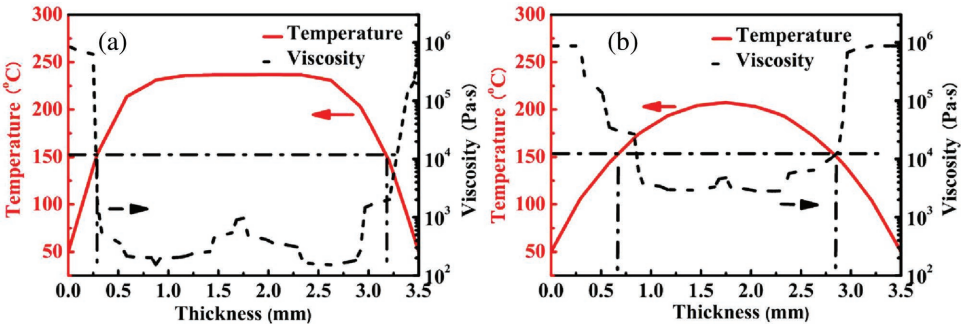

Figure 7. Temperature and viscosity in whole thickness: a) before compression and b) after compression (the parameters are almost the same as the real condition: injection temperature is 230 °C, the dosage of SCF is 0.6%, injection speed is 60 cm^3 s^{-1}, and the shot size is 96%).

that the melt flow had passed the scope of the pressure sensor. The observed temperature peak indicated the end of the filling stage. According to the changes in temperature curves, the pressure curves are divided into different stages, that is, the filling and cooling process.

As shown in Figure 12a, a pressure peak in the packing stage is observed to be lower than that in the filling stage in a conventional injection molding (CIM) cycle. After that, a noticeable negative pressure is observed due to the melt shrinkage at the cooling stage. As shown in Figure 12b, after the filling stage, the expansion of foamed mixture causes a sustained low pressure in cavity, which is much lower than that in the filling stage. The pressure profile in ICMCBF (Figure 12c) is obviously different from others. At the filling stage, the same pressure peak as CIM and CFIM is observed. After the filling stage, however, an extremely high-pressure peak (about 120 bar) is achieved by mold compression and a fast pressure drop is obtained by core-back. These results further verified the expectation that mold compression increased the cavity pressure effectively and core-back induced a fast pressure drop. Based on the analyses in the introduction part, the cell structures have a strong relationship with high cavity pressure and fast pressure drop. During the cooling stage, the expanded mixture of melt and gas induced a pressure in cavity, which was decreased slowly as the melt was cooled down until the mold was open.

Figure 12d shows the highest pressure in the pressure profiles caused by different mold compressions. It can be obviously found that the melt pressure increases with increasing the compression pressure. When the compression pressure is 100 bar, the real pressure in cavity (50.7 bar) cannot re-dissolve the gate-nucleated cells. But when the cavity pressure is up to 110 or 120 bar with the compression pressure of 200 and 300 bar, the fine cell structure can be obtained. In summary, sufficiently high pressure and fast pressure drop contributed to a fine cell structure.

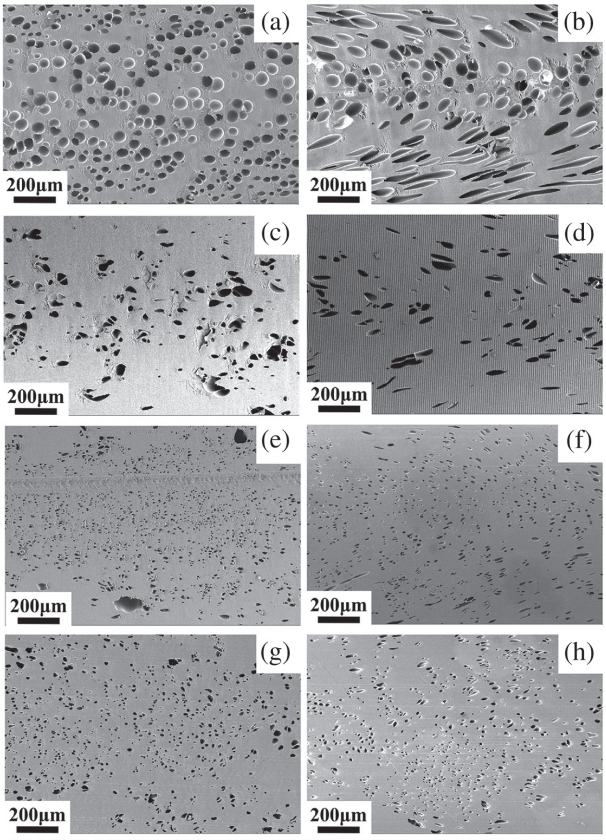

Figure 8. SEM images of ICMCBF samples with compression pressure of a) 0 bar-V, b) 0 bar-P, c) 100 bar-V, d) 100 bar-P, e) 200 bar-V, f) 200 bar-P, g) 300 bar-V, and h) 300 bar-P (V and P indicate the cross sections which are vertical and parallel to the direction of the melt flow) and the compression time is 5 s.

3.5. Mechanical Properties of the CFIM and ICMCBF Foam

Since the fine cell structure and the mechanism of ICMCBF were discussed earlier, the question is whether different cell structures could lead to any difference in the mechanical properties. To answer this question, solid samples and foamed samples under different compression pressures (0, 100, 200, 300 bar) were cut from the injection-molded parts and tested. As shown in **Figure 13**, the mechanical properties of CFIM and ICMCBF samples are closely related to their cell structures, and the tensile and impact strength of ICMCBF are remarkably enhanced than those of CFIM samples. Under loading, a large number of deformed cells and their coalescence in CFIM may become the origination of crack and induce a poor tensile strength than the solid parts. On the contrary, the little un-deformed cells may serve as the function of inactivation

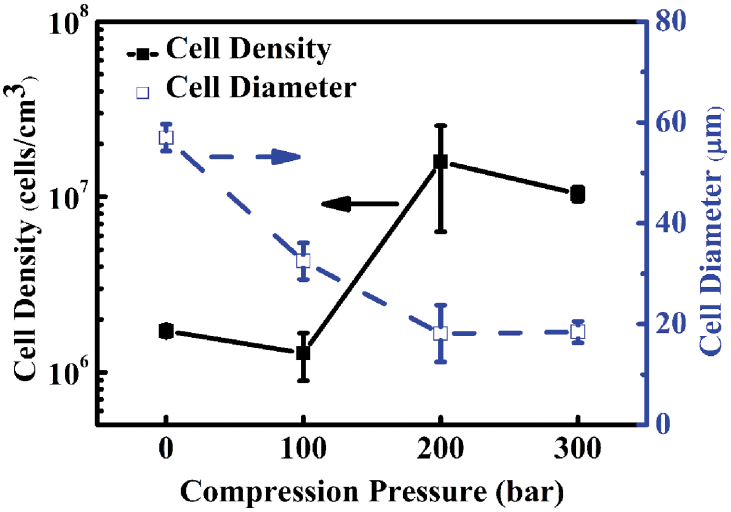

Figure 9. Cell density and cell diameter of ICMCBF samples with different compression pressure (0 bar indicates the CFIM foam) when the compression time is 5 s.

of crack tips which benefits a high mechanical performance. Moreover, the reduced thickness of foamed layer is also important for the increased mechanical strength. On the other hand, higher cell density enhanced the absorption of energy when the samples were under impact. Above all, the structure of ICMCBF with higher cell density, smaller size, uniform size, and reduced foamed layer contributed to a better mechanical performance compared with CFIM. As discussed earlier, when the compression pressure was 100 bar, the foamed layer was much thinner than that in CFIM. This increases the tensile strength. The compression pressure was too low for the re-dissolution of the gate-nucleated cells, and the cells were not as uniform as the samples under 200 and 300 bar. The transformed cells acted as the defects in the part and as stress concentrator.[57] As a result, the impact strength under 100 bar was lower than that under 200 and 300 bar.

In addition, the weight reduction of foam is important when discussing the mechanical property. As discussed earlier, the shot sizes of the CFIM and ICMCBF samples in this article are 96%. This means that the weight reduction of the foamed parts fabricated by different processes is almost the same (including the runner and sprue system). According to the results of the normalized density, the foamed blocks which were cut from CFIM parts showed a smaller density of about 0.85 g cm^{-3} while those cut from ICMCBF parts showed a larger density of about 0.99 g cm^{-3}. Compared with the density of solid PS parts (1.05 g cm^{-3}), the CFIM foam showed a higher weight reduction than ICMCBF. Although lower weight reduction of ICMCBF contributed to the improved mechanical performance than CFIM, the mechanical performance showed a close relationship with the cell structure under the same shot size.

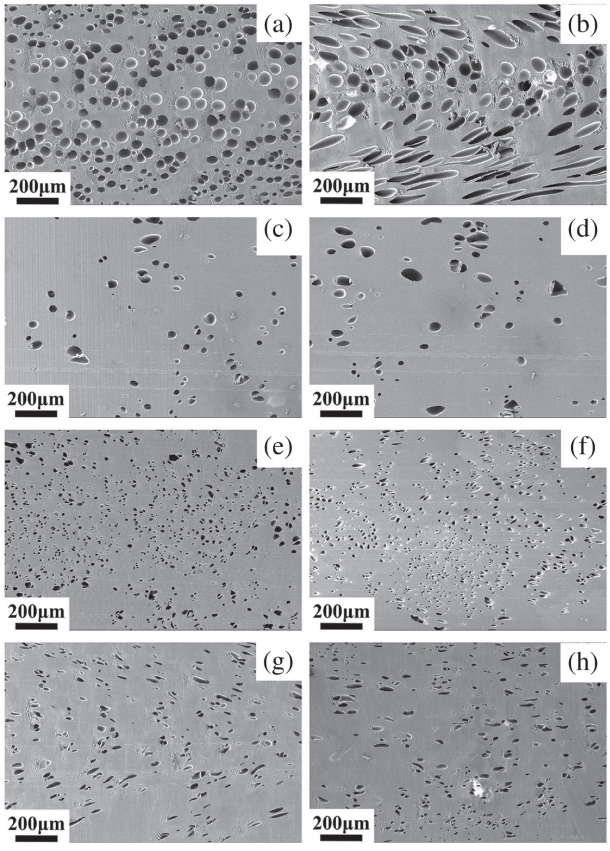

Figure 10. SEM images of ICMCBF samples with compression time of a) 0 s-V, b) 0 s-P, c) 3 s-V, d) 3 s-P, e) 5 s-V, f) 5 s-P, g) 7 s-V, and h) 7 s-P (V and P indicate the cross sections which are vertical and parallel to the direction of the melt flow) and the compression pressure is 300 bar.

4. Conclusion

High-pressure foam injection molding of PS/N_2 was conducted by a new method of combining injection-compression molding with core-back foaming (ICMCBF) technique. The cell structure of ICMCBF, that is, higher density, smaller size, more uniform size distribution, and thinner foamed layer was obviously different from that of the CFIM. The cell structure with various

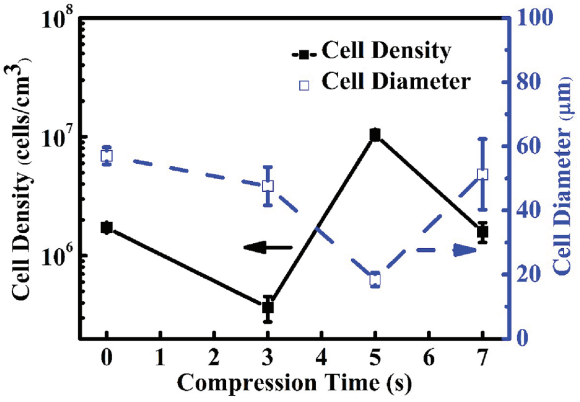

Figure 11. Cell density and cell diameter of ICMCBF samples with different compression times (0 s indicates the CFIM foam) when the compression pressure is 300 bar.

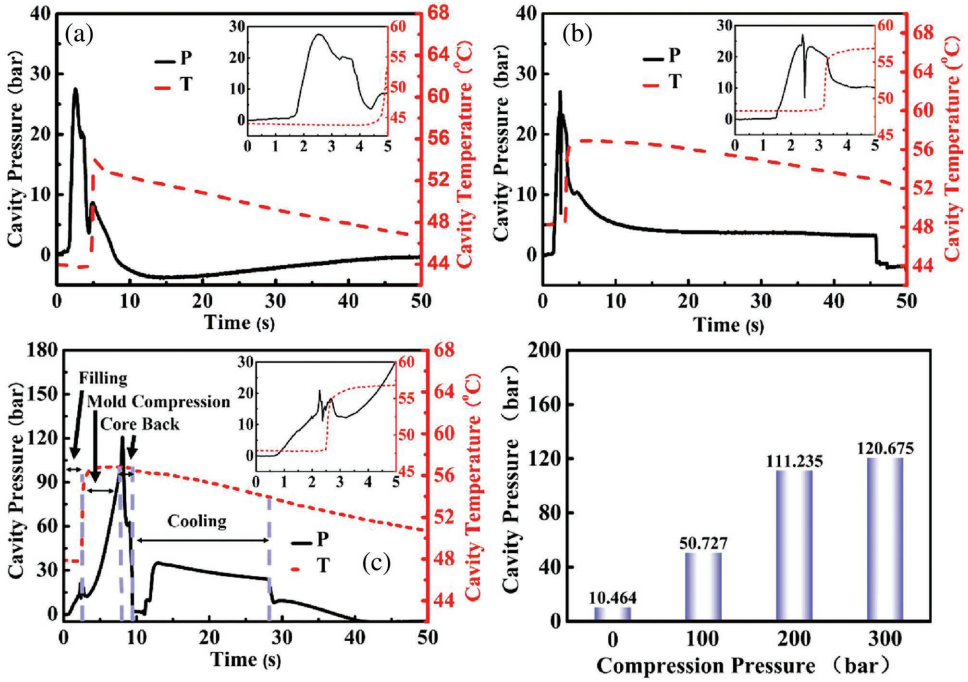

Figure 12. Profiles of temperature and pressure in cavity in a) CIM, b) CFIM, and c) ICMCBF cycles and d) the cavity pressure peak induced by different compression pressures.

compression pressures (0, 100, 200, and 300 bar) and various compression times (0, 3, 5, and 7s) was investigated. When the compression pressure was 200 bar and the compression time was 5 s, the cell density was the highest (1.59×10^7 cells cm^{-3}) and the cell size was the smallest (15 μm). With the help of sensors, the evolution of temperature and pressure in the mold cavity under different injection molding processes was elaborated. The results showed that a high pressure was achieved by mold compression and a quick pressure drop was achieved by core-back technique. In addition, a high cavity pressure and faster pressure drop contributed to the formation of the fine cell structure. Moreover, a close relationship was found between the mechanical property and cell structure. The tensile strength and impact strength of ICMCBF were enhanced by about 60% (from 22.3 to 35.6 MPa) and 80% (from 3.6 to 6.8 MPa), respectively. Although many more studies need to be done, the evolution of cells in HPFIM contributes to the understanding of the nucleation and growth mechanism in the foam injection molding and a new strategy for the fabrication of foam with uniform cell structure is provided. With the addition of unique nanofillers, this process can be potentially used for producing multifunctional polymer nanocomposites to satisfy various applications including energy storage, environmental remediation, electromagnetic interference (EMI) shielding, and sensing.[58–80]

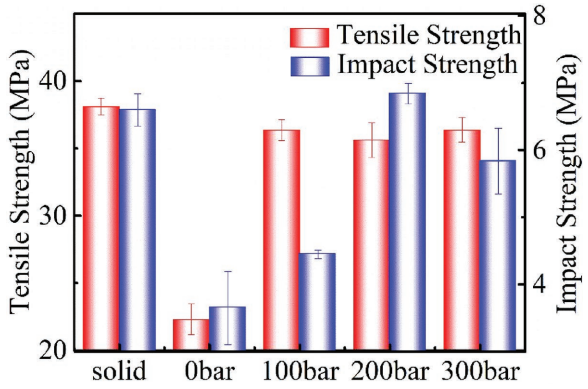

Figure 13. Tensile strength and impact strength for solid and ICMCBF samples with different compression pressures (0 bar indicates the CFIM foam).

Acknowledgements

This work was supported by the Education Department of Henan Provincial (grant number 14A430008); National Natural Science Foundation Item (grant numbers 11572290 and 11432003).

Conflict of Interest

The authors declare no conflict of interest.

Keywords

cell growth, cell nucleation, cell structure, high-pressure foam injection molding, mechanical property

Received: February 17, 2018
Revised: June 8, 2018
Published online: July 23, 2018

[1] X. Liu, Y. Pan, G. Zheng, H. Liu, Q. Chen, C. Liu, J. Zhang, N. Wang, E. K. Wujcik, T. Li, C. Shen, Z. Guo, *Macromol. Mater. Eng.* **2018**, *303*, 1800035.
[2] H. Liu, W. Huang, X. Yang, K. Dai, G. Zheng, C. Liu, C. Shen, X. Yan, J. Guo, Z. Guo, *J. Mater. Chem. C* **2016**, *4*, 4459.
[3] J. Hou, G. Zhao, G. Wang, G. Dong, J. Xu, *Mater. Des.* **2017**, *127*, 115.
[4] H. Liu, J. Guo, W. Huang, K. Dai, G. Zheng, G. C. Liu, C. Shen, X. Yan, J. Guo, Z. Guo, *Nanoscale* **2016**, *8*, 12977.
[5] B. R. B. Kumar, M. Doddamani, S. E. Zeltmann, N. Gupta, M. R. Ramesh, S. Ramakrishna, *Mater. Des.* **2016**, *92*, 414.
[6] H. Liu, M. Dong, W. Huang, J. Gao, K. Dai, J. Guo, G. Zheng, C. Liu, C. Shen, Z. Guo, *J. Mater. Chem. C* **2016**, *5*, 73.
[7] Y. Zhou, B. Su, L. S. Turng, *Cell. Polym.* **2017**, *47*, 51.
[8] H. Liu, W. Huang, J. Gao, K. Dai, G. Zheng, C. Liu, C. Shen, X. Yan, J. Guo, Z. Guo, *Appl. Phys. Lett.* **2016**, *108*, 918.
[9] X. Wang, X. Liu, H. Yuan, H. Liu, C. Liu, T. Li, C. Yan, X. Yan, C. Shen, Z. Guo, *Mater. Des.* **2018**, *139*, 372.
[10] H. Liu, Y. Li, K. Dai, G. Zheng, C. Liu, C. Shen, X. Yan, J. Guo, Z. Guo, *J. Mater. Chem. C* **2016**, *4*, 157.
[11] Y. He, S. Yang, H. Liu, Q. Shao, Q. Chen, C. Lu, Y. Jiang, C. Liu, Z. Guo, *J. Colloid Interface Sci.* **2018**, *517*, 40.
[12] A. Kramschuster, R. Cavitt, D. Ermer, Z. Chen, L. S. Turng, *Polym. Eng. Sci.* **2005**, *45*, 1408.
[13] X. Sun, H. Kharbas, J. Peng, L. S. Turng, *Polymer* **2015**, *56*, 102.
[14] K. A. Seeler, V. Kumar, *J. Reinf. Plast. Compos.* **1993**, *12*, 359.
[15] M. Yuan, L. S. Turng, *Polymer* **2005**, *46*, 7273.
[16] M. Shimbo, I. Higashitani, Y. Miyano, *J. Cell. Plast.* **2016**, *43*, 157.
[17] P. Gong, P. Buahom, M. P. Tran, M. Saniei, C. B. Park, P. Pötschke, *Carbon* **2015**, *93*, 819.
[18] P. Gong, G. Wang, M. P. Tran, P. Buahom, S. Zhai, G. Li, C. B. Park, *Carbon* **2017**, *120*, 1.
[19] J. Gómez-Monterde, M. Schulte, S. Ilijevic, J. Hain, D. Arencón, M. Sánchez-Soto, M. L. Maspoch, *Procedia Eng.* **2015**, *132*, 15.
[20] V. Shaayegan, L. H. Mark, C. B. Park, G. Wang, *AIChE J.* **2016**, *62*, 4035.
[21] S. S. Hwang, S. P. Liu, P. P. Hsu, J. M. Yeh, J. P. Yang, K. C. Chang, S. N. Chu, *Int. Commun. Heat Mass Transfer* **2011**, *38*, 597.
[22] L. Zhang, G. Zhao, G. Wang, G. Dong, H. Wu, *Int. J. Heat Mass Transfer* **2017**, *104*, 1246.
[23] G. L. Wang, G. Q. Zhao, J. C. Wang, L. Zhang, *Polym. Eng. Sci.* **2015**, *55*, 807.
[24] G. Dong, G. Zhao, Y. Guan, G. Wang, X. Wang, *J. Appl. Polym. Sci.* **2014**, *131*, 383.
[25] L. M. Matuana, C. B. Park, J. J. Balatinecz, *Polym. Eng. Sci.* **1998**, *38*, 1862.
[26] M. R. Barzegari, D. Rodrigue, *Polym. Eng. Sci.* **2009**, *49*, 949.
[27] Z. Xu, X. Jiang, T. Liu, G. Hu, L. Zhao, Z. Zhu, W. Yuan, *J. Supercrit. Fluids* **2007**, *41*, 299.
[28] S. Wong, J. W. S. Lee, H. E. Naguib, C. B. Park, *Macromol. Mater. Eng.* **2008**, *293*, 605.
[29] J. W. S. Lee, W. Jing, J. D. Yoon, C. B. Park, *Ind. Eng. Chem. Res.* **2008**, *47*, 9457.
[30] T. Ishikawa, K. Taki, M. Ohshima, *Polym. Eng. Sci.* **2012**, *52*, 875.
[31] R. K. M. Chu, L. H. Mark, D. Jahani, C. B. Park, *J. Cell. Plast.* **2016**, *52*, 619.
[32] J. Zhao, Q. Zhao, C. Wang, B. Guo, C. B. Park, G. Wang, *Mater. Des.* **2017**, *131*, 1.
[33] T. Ishikawa, M. Ohshima, *Polym. Eng. Sci.* **2011**, *51*, 1617.
[34] V. Shaayegan, *eXPRESS Polym. Lett.* **2016**, *10*, 462.
[35] V. Shaayegan, G. Wang, C. B. Park, *Chem. Eng. Sci.* **2016**, *155*, 27.
[36] V. Shaayegan, G. Wang, C. B. Park, *Eur. Polym. J.* **2016**, *76*, 2.
[37] S. Pilla, A. Kramschuster, L. Yang, J. Lee, S. Gong, L. S. Turng, *Mat. Sci. Eng., C* **2009**, *29*, 1258.
[38] C. A. Villamizar, C. D. Han, *Polym. Eng. Sci.* **1978**, *18*, 699.
[39] A. Ameli, P. U. Jung, C. B. Park, *Carbon* **2013**, *60*, 379.
[40] A. Ameli, M. Nofar, D. Jahani, G. Rizvi, C. B. Park, *Chem. Eng. J.* **2015**, *262*, 78.
[41] A. Ameli, M. Nofar, S. Wang, C. B. Park, *ACS Appl. Mater. Interfaces* **2014**, *6*, 11091.
[42] A. Ameli, P. U. Jung, C. B. Park, *Compos. Sci. Technol.* **2013**, *76*, 37.
[43] V. Shaayegan, C. Wang, F. Costa, S. Han, C. B. Park, *Eur. Polym. J.* **2017**, *92*, 314.
[44] K. Nagato, *Polymers* **2014**, *6*, 604.
[45] N. H. Kim, A. I. Isayev, *Polym. Eng. Sci.* **2013**, *53*, 1786.
[46] H. P. Heim, M. Tromm, *Polymer* **2015**, *56*, 111.
[47] J. Zhao, Q. Zhao, L. Wang, C. Wang, B. Guo, C. B. Park, G. Wang, *Eur. Polym. J.* **2018**, *98*, 1.
[48] H. X. Huang, J. D. Tian, W. S. Guan, *Polym. Eng. Sci.* **2014**, *54*, 327.
[49] H. J. Oh, Y. S. Song, *RSC Adv.* **2017**, *7*, 14302.
[50] X. Zhuang, J. Ouyang, Y. Li, C. Jiang, L. Wang, *Appl. Therm. Eng.* **2018**, *128*, 1391.
[51] S. N. Leung, A. Wong, Q. Guo, C. B. Park, J. H. Zong, *Chem. Eng. Sci.* **2009**, *64*, 4899.
[52] Z. Xi, J. Chen, T. Liu, L. Zhao, L. S. Turng, *Chin. J. Chem. Eng.* **2016**, *24*, 180.
[53] J. Gómez-Monterde, M. Sánchez-Soto, M. L. Maspoch, *Composites, Part A* **2017**, *104*, 1.
[54] A. Ameli, M. Nofar, C. B. Park, P , Pötschke, G. Rizvi, *Carbon* **2014**, *71*, 206.
[55] Y. Sun, Y. Ueda, H. Suganaga, M. Haruki, S. I. Kihara, S. Takishima, *J. Supercrit. Fluids* **2015**, *103*, 38.
[56] Y. Sun, Y. Ueda, H. Suganaga, M. Haruki, S. I. Kihara, S. Takishima, *J. Supercrit. Fluids* **2015**, *107*, 733.
[57] A. N. J. Spörrer, V. Altstädt, *J. Cell. Plast.* **2007**, *43*, 313.
[58] K. Sun, P. Xie, Z. Wang, T. Su, J. Shao, J. Ryu, X. Zhang, J. Guo, A. Shankar, J. Li, R. Fan, D. Cao, Z. Guo, *Polymer* **2017**, *125*, 50.
[59] Y. Ma, L. Lyu, Y. Guo, Y. Fu, Q. Shao, T. Wu, S. Guo, K. Sun, X. Guo, E. K. Wujcik, Z. Guo, *Polymer* **2017**, *128*, 12.
[60] Y. Wang, P. Zhou, S. Luo, S. Guo, J. Lin, Q. Shao, X. Guo, Z. Liu, J. Shen, B. Wang, Z. Guo, *Adv. Poly. Technol.* **2018**, in press, https://doi.org/10.1002/adv.21969
[61] J. Zhao, L. Wu, C. Zhan, Q. Shao, Z. Guo, L. Zhang, *Polymer* **2017**, *133*, 272.
[62] C. Wang, B. Mo, Z. He, C. X. Zhao, L. Zhang, Q. Shao, X. Guo, E. Wujcik, Z. Guo, *Polymer* **2018**, *138*, 363.
[63] C. Wang, B. Mo, Z. He, Q. Shao, D. Pan, E. Wujick, J. Guo, X. Xie, X. Xie, Z. Guo, *J. Membrane Sci.* **2018**, *556*, 118.
[64] Z. Hu, Q. Shao, Y. Huang, L. Yu, D. Zhang, X. Xu, J. Lin, H. Liu, Z. Guo, *Nanotechnology* **2018**, *29*, 185602.
[65] K. Sun, R. Fan, X. Zhang, Z. Zhang, Z. Shi, N. Wang, P. Xie, Z. Wang, G. Fan, H. Liu, C. Liu, T. Li, C. Yan, Z. Guo, *J. Mater. Chem. C* **2018**, *6*, 2925.
[66] Y. Guo, G. Xu, X. Yang, K. Ruan, T. Ma, Q. Zhang, J. Gu, Y. Wu, H. Liu, Z. Guo, *J. Mater. Chem. C* **2018**, *6*, 3004.
[67] C. Wang, Z. He, X. Xie, X. Mai, Y. Li, T. Li, M. Zhao, C. Yan, H. Liu, E. Wujcik, Z. Guo, *Macromol. Mater. Eng.* **2018**, *303*, 1700462.
[68] J. Lin, X. Chen, C. Chen, J. Hu, C. Zhou, X. Cai, W. Wang, C. Zheng, R. Zhang, J. Cheng, H. Liu, Z. Guo, *ACS Appl. Mater. Interfaces* **2018**, *10*, 6124.
[69] Y. Li, B. Zhou, G. Zheng, X. Liu, T. Li, C. Yan, C. Cheng, K. Dai, C. Liu, C. Shen, Z. Guo, *J. Mater. Chem. C* **2018**, *6*, 2258.
[70] X. Guan, G. Zheng, K. Dai, C. Liu, X. Yan, C. Shen, Z. Guo, *ACS Appl. Mater. Interfaces* **2016**, *8*, 14150.
[71] L. Lv, J. Liu, H. Liu, C. Liu, Y. Lu, K. Sun, R. Fan, N. Wang, N. Lu, Z. Guo, E. Wujcik, *Eng. Sci.* **2018**, *2*, 120.

[72] C. Hu, Z. Li, Y. Wang, J. Gao, K. Dai, G. Zheng, C. Liu, C. Shen, H. Song, Z. Guo, *J. Mater. Chem. C* **2017**, *5*, 2318.
[73] L. Yan, H. Wang, D. Huang, H. Luo, *Eng. Sci.* **2018**, *1*, 4. http://www.espublisher.com/doi/10.30919/es.180318
[74] W. Zhao, Z. Shi, S. Hu, G. Yang, H. Tian, *Adv. Compos. Hybrid Mater.* **2018**, *1*, 320.
[75] C. Wang, Z. He, X. Xie, X. Mai, Y. Li, T. Li, M. Zhao, C. Yan, H. Liu, E. Wujcik, Z. Guo, *Macromol. Mater. Eng.* **2018**, *3*, 1700462.
[76] C. Wang, Y. Wu, Y. Li, Q. Shao, X. Yan, C. Han, Z. Wang, Z. Liu, Z. Guo, *Polym. Adv. Technol.* **2018**, *29*, 668.
[77] Y. Guo, Y. Li, X. Lou, J. Guan, Y. Li, X. Mai, H. Liu, C. X. Zhao, N. Wang, C. Yan, J. Dai, R. Su, Z. Guo, *J. Mater. Sci.* **2018**, in press, https://doi.org/10.1007/s10853-018-2229-0
[78] H. Du, C. Zhao, J. Lin, Z. Hu, Q. Shao, J. Guo, B. Wang, D. Pan, E. K. Wujcik, Z. Guo, *Chem. Record* **2018**, *18*, 1.
[79] Y. Pan, D. W. Schulbert, J. E. Ryu, E. Wujcik, C. Liu, C. Shen, X. Liu, *Eng. Sci.* **2018**, *1*, 86. http://espublisher.com/doi/10.30919/es.180402
[80] B. Zhou, Y. Li, K. Dan, G. Zheng, C. Liu, Y. Ma, J. Zhang, N. Wang, C. Shen, Z. Guo, *J. Mater. Chem. C* **2018**, in press, https://doi.org/10.1039/C8TC01779D